

Resolving the ξ Boo Binary with *Chandra*, and Revealing the Spectral Type Dependence of the Coronal “FIP Effect”

Brian E. Wood¹, Jeffrey L. Linsky²

ABSTRACT

On 2008 May 2, *Chandra* observed the X-ray spectrum of ξ Boo (G8 V+K4 V), resolving the binary for the first time in X-rays and allowing the coronae of the two stars to be studied separately. With the contributions of ξ Boo A and B to the system’s total X-ray emission now observationally established (88.5% and 11.5%, respectively), consideration of mass loss measurements for GK dwarfs of various activity levels (including one for ξ Boo) leads to the surprising conclusion that ξ Boo B may dominate the wind from the binary, with ξ Boo A’s wind being very weak despite its active corona. Emission measure distributions and coronal abundances are computed for both stars and compared with *Chandra* measurements of other moderately active stars with G8-K5 spectral types, all of which exhibit a narrow peak in emission measure near $\log T = 6.6$, indicating that the coronal heating process in these stars has a strong preference for this temperature. As is the case for the Sun and many other stars, our sample of stars shows coronal abundance anomalies dependent on the first ionization potential (FIP) of the element. We see no dependence of the degree of “FIP effect” on activity, but there is a dependence on spectral type, a correlation that becomes more convincing when moderately active main sequence stars with a broader range of spectral types are considered. This clear dependence of coronal abundances on spectral type weakens if the stellar sample is allowed to be contaminated by evolved stars, interacting binaries, or extremely active stars with $\log L_X > 29$, explaining why this correlation has not been recognized in the past.

Subject headings: stars: individual (ξ Boo) — stars: coronae — stars: late-type — X-rays: stars

¹Naval Research Laboratory, Space Science Division, Washington, DC 20375; brian.wood@nrl.navy.mil

²JILA, University of Colorado and NIST, Boulder, CO 80309-0440; jlinsky@jila.colorado.edu

1. INTRODUCTION

At a distance of only 6.7 pc, the primary of the ξ Boo binary system, ξ Boo A (G8 V), is one of the two brightest “moderately active” coronal X-ray sources in the sky. The only star of this coronal activity level with a comparable X-ray flux at Earth is ϵ Eri (K2 V, $d = 3.2$ pc). As such, these two stars are of crucial importance for establishing the coronal properties of stars that are significantly more active than the Sun, but which are not in the extremely active regime that would be represented by the RS CVn binaries or very young stars with rotation periods of only a few days.

Drake et al. (2000) find that the coronal emission measure (EM) distributions of ϵ Eri and ξ Boo are similar to those of bright active regions on the Sun. They note that the X-ray emission from these stars can therefore be explained by stellar surfaces that are completely covered with solar-like active regions, suggesting that ϵ Eri and ξ Boo A represent a maximum of solar-like activity for coronal stars, whereas stars with even higher X-ray luminosities and higher coronal temperatures represent a completely different regime of coronal activity. This interpretation places ϵ Eri and ξ Boo A at an interesting coronal transition point.

Further evidence that ϵ Eri and ξ Boo A lie near a transition in the nature of coronal activity comes from stellar wind measurements, which are based on analyses of H I Ly α absorption from wind-ISM interaction regions (Wood et al. 2005a). At low activity levels mass loss increases with activity, with ϵ Eri having a mass loss rate 30 times that of the Sun (i.e., $\dot{M} = 30 \dot{M}_{\odot}$, where $\dot{M}_{\odot} = 2 \times 10^{-14} \text{ M}_{\odot} \text{ yr}^{-1}$). However, the somewhat more active ξ Boo system has a surprisingly weak wind with only $5 \dot{M}_{\odot}$, leading to the suggestion that the observed increase of mass loss with activity ends abruptly at an X-ray surface flux of about $F_X = 1 \times 10^6 \text{ ergs cm}^{-2} \text{ s}^{-1}$, with ϵ Eri and ξ Boo on opposite sides of this dividing line (Wood et al. 2005a).

The wind measurements suggest a slight modification of the proposal that ϵ Eri and ξ Boo A represent an extreme of truly solar-like activity. They suggest that ϵ Eri is the true extreme, while ξ Boo A actually lies beyond it at the low end of the non-solar-like activity regime. Evidence that ξ Boo A’s magnetic topology is fundamentally different from the Sun comes from spectropolarimetric measurements of photospheric fields on ξ Boo A. Petit et al. (2005) find evidence for both a global dipole field component much stronger than that of the Sun (~ 40 G), and a strong toroidal field component (~ 120 G) that has no clear solar analog. We also note that the activity level of ξ Boo A is roughly where one starts to see polar starspots (Strassmeier 2002), which also have no solar analog. Toner & Gray (1988) find evidence for high latitude spots on ξ Boo A, though not necessarily “polar spots.” Perhaps the strong large-scale fields found by Petit et al. (2005) envelope the star and inhibit wind flow, explaining why ξ Boo’s wind is surprisingly weak. Consistent with

this idea, Petit et al. (2008) present evidence that as stellar rotation and magnetic activity increase, stars tend to store a larger fraction of their magnetic energy in large scale fields, which could in principle inhibit mass loss.

With this background in mind, we here present an analysis of the X-ray spectrum of ξ Boo A based on new observations from *Chandra*, with the goal of seeing whether the apparent changes in coronal character noted above find clear expression in the coronal spectrum of ξ Boo A, and coronal properties inferred from it. A similar spectrum of ϵ Eri has already been analyzed, so a central goal of this paper is to compare the ξ Boo A spectrum with that of ϵ Eri and similar stars (Wood & Linsky 2006, hereafter WL06).

Other coronal spectra of ξ Boo have been obtained by previous X-ray and EUV missions (e.g., Laming & Drake 1999; Pandey & Srivastava 2009), but the new *Chandra* data are superior in many ways. One of them is that *Chandra*/LETGS observations allow the X-ray spectrum to be observed at high spectral resolution over a very broad spectral range of 5 – 175 Å. This allows the detection of many coronal emission lines that have never been previously detected before from ξ Boo A.

Another particularly important improvement is that *Chandra*’s superb spatial resolution allows us for the first time to truly address the issue of ξ Boo’s binarity. For ξ Boo A has a companion, ξ Boo B (K4 V), which is only 6'' away, and *no X-ray or UV observation of ξ Boo has ever truly resolved the binary*. Table 1 lists various properties of the two ξ Boo stars. The faster rotation and larger size of the primary lead to the expectation that ξ Boo A should dominate the coronal emission from the system. Detailed analyses of IUE data and a ROSAT/HRI image of ξ Boo do indeed suggest that ξ Boo A dominates the binary’s UV and X-ray emission (Hartmann et al. 1979; Schmitt 1997), so the usual assumption of simply assigning all flux to the primary should be a decent approximation. However, ξ Boo B’s spectral type and rotation period are not that different from the X-ray luminous ϵ Eri (K2 V; $P_{rot} = 11.7$ days). Thus, ξ Boo B should be contributing a non-negligible flux to the system’s total X-ray emission. The older observations simply do not have sufficient spatial resolution to quantify how much. In short, the new *Chandra* data presented here allow the first X-ray detection of ξ Boo B, and they ensure that the brighter spectrum of ξ Boo A is uncontaminated by any emission from the companion.

2. OBSERVATIONS AND DATA REDUCTION

The ξ Boo binary was observed on 2007 May 2 for 97.2 ksec with *Chandra*’s LETGS configuration, combining the Low Energy Transmission Grating (LETG) and the component

of the High Resolution Camera detector intended for use in spectroscopy (HRC-S). The zeroth-order LETGS image of ξ Boo is displayed in Figure 1, showing how cleanly the stars are separated in the *Chandra* data, representing the first resolution of the binary in X-rays. We measure a position angle and stellar separation for the binary of $\theta = 310.9^\circ$ and $\rho = 6.30''$, respectively, in reasonable agreement with the $\theta = 310.1^\circ$ and $\rho = 6.15''$ values expected from the system’s orbital elements (Söderhjelm 1999). The zeroth order image provides the simplest way to measure the contribution of each star to ξ Boo’s total X-ray emission. The primary dominates the emission from the system, accounting for 88.5% of the total counts.

We also use the zeroth order image to assess the variability of the two stars during the course of the daylong observation. Figure 2 shows light curves for the two ξ Boo components, indicating significant variability for both stars. For ξ Boo A, there appears to be a long duration flare near the beginning of the observation, and a much shorter duration event later on. In extracting spectra from the raw *Chandra* data, we initially tried to separate flaring and quiescent times. However, we were unable to discern any clear differences between the resulting noisy flare spectrum and that of quiescence. Thus, in the final spectral extraction procedure described below, we simply extract a single spectrum for each star, including both quiescent and flaring times.

The standard pipeline processing of LETGS data does not properly separate the spectra of the two stars, so the spectral extraction must be performed in a more manual fashion. In a previous paper we have described in detail how we extracted separate LETGS spectra of stars in two other binary systems, 36 Oph and 70 Oph (WL06). We follow a very similar procedure here, which is now described in abbreviated form.

The data are processed using version 4.1.2 of the CIAO software. The processing includes a removal of background counts using the standard “light” pulse height background filter available in CIAO, but we also account for time-dependent gain corrections using software outside of CIAO, corrections which would later be added to a subsequent official CIAO release (version 4.2). By reducing background counts from our data, this filtering significantly improves the signal-to-noise of our final spectra.

The processing initially yields a zeroth order image of the target at the aimpoint, which we have already discussed (see Fig. 1), and two essentially identical spectra dispersed in opposite directions along the long axis of the HRC-S detector, a plus order and a minus order spectrum. The spatial resolution in the cross-dispersion direction worsens at long wavelengths where the spectrum is furthest from the focal point. We use a conservatively broad source extraction window with a width of 25 pixels centered on each stellar spectrum for $\lambda < 90 \text{ \AA}$. The window is broadened for $\lambda > 90 \text{ \AA}$. To avoid overlapping source windows,

for each star we expand the window only in the direction away from its companion star by 30 pixels. At the longest wavelengths, we have to accept that there is some small degree of unresolvable blending. We use 90 pixel background windows on each side of the stellar spectra to determine a wavelength dependent background to subtract from the spectra of the two stars. Finally, the plus and minus order spectra are coadded to yield the final product shown in Figure 3.

3. IMPLICATIONS FOR ξ BOO’S WIND MEASUREMENT

The clear separation of the ξ Boo binary allows the first precise and unambiguous measurement of the X-ray luminosity of both stars. The system’s X-ray luminosity reported in the ROSAT all-sky survey is $\log L_X = 28.91$ (Schmitt & Liefke 2004). Dividing this emission between ξ Boo’s two stars according to the contribution ratio suggested by Figure 1 yields the ROSAT X-ray luminosities reported in Table 1.

This new knowledge of the coronal activity of both ξ Boo stars has interesting ramifications for the interpretation of ξ Boo’s wind measurement. As mentioned in §1, ξ Boo has a measured wind strength of $5 \dot{M}_\odot$, but the measurement is for the combined wind of the system, and there is no way to tell from the observations the contribution of each star to this total (Wood et al. 2005a). Figure 4 plots mass loss rate as a function of coronal X-ray emission for all main sequence stars with measured winds, analogous to a figure from Wood et al. (2005a). But in this figure we plot separate points for ξ Boo A and ξ Boo B, for three different assumptions about how the collective wind is divided between the two stars.

We now know for a fact that ξ Boo B is very similar to ϵ Eri, 36 Oph, and 70 Oph in terms of its coronal activity. But these stars all have rather high mass loss rates. The only way that ξ Boo B can be consistent with even the weakest of these winds, that of 36 Oph, is if ξ Boo B accounts for practically all of ξ Boo’s wind. This would leave the more active ξ Boo A with a wind that is possibly weaker than that of the Sun, despite its active corona, strengthening the case for the existence of a wind dividing line near an X-ray surface flux of $F_X = 1 \times 10^6 \text{ ergs cm}^{-2} \text{ s}^{-1}$ (see Fig. 4), where stronger large scale magnetic fields begin to inhibit mass loss. Even if ξ Boo A accounts for nearly all of the binary’s wind, it would still be weak compared to that of ϵ Eri, and then one would have to explain why ξ Boo B apparently has a wind over an order of magnitude weaker than that of many other stars of equal activity.

We come to the surprising conclusion that the most likely interpretation of the available data is that ξ Boo B dominates the wind of the ξ Boo system. This conclusion is also

consistent with the idea that a wind dividing line exists at an X-ray surface flux of about $F_X = 1 \times 10^6 \text{ ergs cm}^{-2} \text{ s}^{-1}$ (see §1), separating less active stars with strong winds and more active stars with weaker winds (Wood et al. 2005a; Wood 2004). This activity dependent wind dividing line is not to be confused with the spectral type dependent wind-corona dividing line long known to exist for red giant stars (Linsky & Haisch 1979). It must be noted that our conclusions rely on a very limited number of wind detections. Further support for these interpretations should be sought from more wind measurements of main sequence stars, particularly for active stars.

4. SPECTRAL ANALYSIS

4.1. Line Identification and Measurement

We use version 6.0 of the CHIANTI atomic database to identify emission lines in our spectra (Dere et al. 1997, 2009). The identified lines are shown in Figure 3 and listed in Table 2. Table 2 lists counts for the detected lines, measured by direct integration from the spectra. Line formation temperatures are quoted in the third column of the table, based on maxima of contribution functions computed using the ionization equilibrium computations of Arnaud & Rothenflug (1985). Uncertainties quoted in Table 2 are 1σ . For the fainter ξ Boo B source, only the strongest lines are detected, but we quote 2σ upper limits for the nondetections, based on summing in quadrature the uncertainties in 5 bins surrounding the location of the line, and then multiplying this sum by two.

Measurements are made for all lines that appear visually to be at least marginally detected. However, cases in which the uncertainty implies a $< 2\sigma$ detection must be considered questionable. After the emission measure analysis described in §4.4 is completed, we confirm *a posteriori* that these questionable detections are at least plausible based on the derived emission measure distributions and abundances, which are constrained primarily by the stronger emission lines in the analysis.

Many of the emission lines are blends. We list in Table 2 all lines that we believe contribute a significant amount of flux to the feature based on the line strengths in the CHIANTI database. This determination is reassessed after EM distributions are estimated, and model spectra can be computed from them and compared with the data. A few of the features identified in Figure 3 are blends of lines of different species (see Table 2). Although we measure counts for these blends and list them in the table, these measurements are not used in the emission measure analysis.

4.2. Coronal Densities

Coronal electron densities can be estimated for the two ξ Boo stars directly from the O VII $\lambda 21.8$ line measurements in Table 2. There are in fact several He-like triplets in the observed spectral range that are useful for density measurements: Si XIII $\lambda 6.7$, Mg XI $\lambda 9.2$, Ne IX $\lambda 13.6$, and O VII $\lambda 21.8$. However, insufficient spectral resolution, low signal-to-noise, and blending issues complicate any attempt to use the Si XIII, Mg XI, and Ne IX lines for this purpose (Ness et al. 2002). For this reason, we focus only on the stronger, better separated O VII lines here.

The specific line ratio of interest is that of the forbidden line to the intersystem line: $f/i \equiv \lambda 22.101/\lambda 21.807$. Using the results of collisional equilibrium models from Porquet et al. (2001), the measured line ratios for ξ Boo A and ξ Boo B translate to upper limits of $\log n_e < 10.24$ and $\log n_e < 11.43$, respectively, as reported in Table 3. The ξ Boo A limit is consistent with values that Lamington & Drake (1999) estimate from EUVE spectra. Densities of about $\log n_e \approx 10$ are consistent with spectra of ϵ Eri, 36 Oph AB, and 70 Oph AB as well, which have activity levels similar to that of the ξ Boo stars (WL06). Thus, there is no clear evidence for coronal density differences among moderately active stars observed by *Chandra*.

4.3. Comparing the Line Fluxes of ξ Boo A and ϵ Eri

Among moderately active GK dwarfs with intrinsic X-ray luminosities of $\log L_X = 28 - 29$, the two easiest to observe from Earth are ξ Boo A (G8 V) and ϵ Eri (K2 V), due to their close proximity. We can see how the coronal temperatures and abundances of these two key stars compare simply by plotting ratios of their coronal line luminosities as a function of line formation temperature, as is done in Figure 5. The ξ Boo A line luminosities in the figure originate from the line counts measured in Table 2. The ϵ Eri luminosities are computed from line counts similarly listed in WL06.

Figure 5 shows that nearly all the line ratios are above one at all temperatures, indicative of ξ Boo A being the more active star. The ratios are clearly temperature dependent, with the ratio rising from ~ 1.5 at $\log T = 6.0$ to ~ 5 at $\log T = 7.0$. This implies a hotter corona for the more active ξ Boo A. This is consistent with previous observations demonstrating correlations between coronal activity and coronal temperature (Güdel et al. 1997; Güdel 2004; Telleschi et al. 2005). It is intriguing how smoothly and linearly the line ratios rise with temperature.

The lines in Figure 5 are divided into those with low first ionization potential (FIP) and

those with high FIP. In the solar corona and solar wind, elemental abundances are found to be dependent on FIP. Relative to the photosphere, elements with low FIP (Fe, Mg, Si, etc.) are generally found to have coronal abundances that are enhanced relative to elements with high FIP (C, N, O, Ne, etc.) (Feldman & Laming 2000). Evidence for this effect has been found for some stars of low to moderate activity (Laming et al. 1996; Drake et al. 1997; Laming & Drake 1999). However, on very active stars the FIP effect tends to be either absent, or sometimes an inverse FIP effect is observed, where low-FIP elements have coronal abundances that are *lower* than photospheric (Audard et al. 2001, 2003; Brinkman et al. 2001; Güdel et al. 2001; Huenemoerder et al. 2001, 2003; Sanz-Forcada et al. 2003, 2009; Ball et al. 2005).

Thus, for main sequence stars the picture is of the FIP effect generally decreasing as activity increases (Telleschi et al. 2005). But there are exceptions to this trend, and Figure 5 is itself inconsistent with a tight correlation between activity and FIP effect, as the lower flux ratios of the high-FIP ions in Figure 5 demonstrate that ξ Boo A’s corona exhibits a stronger FIP effect than the less active ϵ Eri. We will return to this issue in §4.6.

4.4. Emission Measure Analysis

In order to quantify the coronal abundances and temperature distributions, we perform an emission measure analysis for ξ Boo A and B based on our measurements of their coronal emission lines. The EM analysis uses version 2.6 of the PINTofALE software developed by Kashyap & Drake (1998, 2000). This analysis follows closely that of WL06 in our study of LETGS spectra from ϵ Eri, 36 Oph, and 70 Oph, so we do not describe it again in great detail here.

Figure 6 shows EM distributions (in units of cm^{-3}) for the two ξ Boo stars, and compares them with distributions that we previously computed for five other moderately active G8-K5 dwarfs (WL06). These distributions are computed using CHIANTI emissivities (Dere et al. 1997, 2009), and ionization balance calculations from Mazzotta et al. (1998). Our line measurements are corrected for interstellar absorption, but the interstellar H column densities towards these stars, including ξ Boo (see Table 1), are low enough that this is not an important correction.

For elements with detected lines we can compute coronal abundances in the EM analysis. However, line measurements alone only allow *relative* abundances to be computed, and only the shape of the EM distribution can be inferred as opposed to its absolute value. Initially, we assume a solar photospheric abundance for Fe from Grevesse & Sauval (1998), and all

other abundances are computed relative to Fe. The derived ξ Boo abundance ratios are listed in Table 3.

In order to compute an *absolute* Fe abundance, and to properly normalize the EM distribution, the line-to-continuum ratio must be assessed. Figure 7 illustrates this process for the case of ξ Boo A. The figure shows a synthetic spectrum generated from the emission measure distribution in Figure 6, assuming an absolute Fe abundance of $[\text{Fe}/\text{H}] = 0.7[\text{Fe}/\text{H}]_{\odot}$, which is judged to lead to the best fit. This is the same as the ratio found for ϵ Eri (WL06). For ξ Boo B, we find a similar value of $[\text{Fe}/\text{H}] = 0.8[\text{Fe}/\text{H}]_{\odot}$ (see Table 3). These results are used to properly normalize the EM distributions in Figure 6. Figure 3 displays synthetic spectra of ξ Boo A and B based on the EM distributions. In addition to the dominant first-order spectrum, we also take into account orders 2–5 in generating synthetic spectra. Both Figures 3 and 7 explicitly show the contributions of these higher orders to the total spectrum.

In logarithmic terms, our measurement for ξ Boo A implies $\log[\text{Fe}/\text{Fe}_{\odot}] = -0.15$, where Fe_{\odot} is here the solar photospheric abundance of Fe. This measurement can be compared with the $\log[\text{Fe}/\text{Fe}_{\odot}] = 0.1^{+0.2}_{-0.15}$ measurement of Drake & Kashyap (2001) based on EUVE spectra. At this point it is worth noting that the contributions of weak, unresolved, and unidentified lines to the observed “continuum” could easily lead to underestimates of $[\text{Fe}/\text{H}]$, so our $[\text{Fe}/\text{H}]$ measurements could be conservatively regarded as lower limits. Given that our measurement is lower than that of Drake & Kashyap (2001), perhaps there are more lines missing and unaccounted for within the LETGS spectral region than in the EUVE spectral region analyzed by Drake & Kashyap (2001), presumably leading to an underestimate of $[\text{Fe}/\text{H}]$ on our part. Nevertheless, both our measurement and that of Drake & Kashyap (2001) show a higher Fe abundance in the corona than in the photosphere, where $\log[\text{Fe}/\text{Fe}_{\odot}] = -0.26$ (see Table 1), consistent with a solar-like FIP effect (see §4.3). In following sections that focus on comparing the coronal abundances of different stars, we avoid the systematic errors involved in computing absolute abundances by comparing only relative abundances, specifically abundances relative to Fe.

The seven EM distributions in Figure 6 are superficially similar in appearance, with a dramatic rise at about $\log T = 6.0$. But perhaps the most interesting feature is that all of the distributions show an EM peak near $\log T = 6.6$, a peak that is particularly convincing for the two brightest stars, ξ Boo A and ϵ Eri. The coronal heating on these moderately active stars seems to favor this particular temperature.

The EM distribution that Laming & Drake (1999) derived for ξ Boo A from EUVE data agrees nicely with our *Chandra* distribution. Their peak at $\log T = 6.6$ is not quite as narrow or prominent, but this may just be a result of the ion-by-ion method that Laming & Drake

(1999) use to quantify their emission measures. As there is some overlap in the EUVE and *Chandra*/LETGS spectra in the 80 – 175 Å range, there are some lines in common to these two analyses. The most precise way to compare the activity level of ξ Boo A during the EUVE and LETGS observations is to directly compare the line fluxes rather than the derived EM distributions. The LETGS/EUVE line flux ratios have a weighted mean and standard deviation of 0.75 ± 0.28 .

An assessment of the relative flux calibration of EUVE and LETGS by Beuermann et al. (2006) using white dwarf spectra suggests calibration errors in the opposite direction, with LETGS/EUVE ratios of 1.15 ± 0.07 . Another systematic error that works in the opposite direction is the fact that, unlike LETGS, the EUVE fluxes will be contaminated by emission from ξ Boo B. Thus, the below unity value of the average LETGS/EUVE line ratio for ξ Boo A is likely indicative of genuine stellar variability, with the star being somewhat fainter during the LETGS observation. However, the very modest level of variability suggested by the LETGS/EUVE comparison is hardly surprising, as the coronal emissions of cool main sequence stars are known to be quite variable on all kinds of timescales.

Finally, we can compute broadband X-ray luminosities directly from the LETGS spectra. We first subtract the higher order contributions to the spectra estimated from the EM analysis (i.e., the green line in Figure 7). We can then combine the corrected spectra with the known first order effective area curve and exposure time to convert counts in our spectra to fluxes. From the flux spectra we can compute X-ray luminosities for any wavelength region within the spectrum. In Table 1, we list luminosities computed in this way for the ROSAT-like 0.1 – 2.4 keV (5 – 120 Å) bandpass. The total ξ Boo system luminosity of $\log L_X = 28.98$ computed in this way agrees reasonably well with the ROSAT all-sky survey measurement of $\log L_X = 28.91$ (Schmitt & Liefke 2004). The first order spectra suggest ξ Boo A accounts for about 84.6% of ξ Boo’s total X-ray flux, compared to the 88.5% contribution to counts in the zeroth order image. The discrepancy is due in part to the difference between count measurements and flux, the latter of which requires consideration of the effective area of the instrument. The discrepancy is also due in part to differences in the effective areas for the zeroth order image and first order spectra.

4.5. Coronal Abundances

In §4.4, we compared the EM distributions of seven moderately active G8-K5 dwarfs observed with LETGS. We also wish to compare the coronal abundances of these seven stars, in order to first determine if a FIP effect exists for these stars, and if so to then compare its magnitude within this stellar sample. Our calculation of abundances in the EM analysis

assumes that abundances are the same at all temperatures throughout the corona. Figure 5 suggests that this is probably a good assumption, as it shows that the differential FIP effect between ξ Boo A and ϵ Eri is the same throughout the $\log T = 6.1 - 6.9$ temperature range that dominates the coronal emission measure distributions of these stars.

Figure 8 compares the coronal abundances of our sample of stars, plotting the abundances relative to Fe, as listed in Table 3. But the search for a FIP effect relies on knowing not just the coronal abundance by itself, but the coronal abundance relative to the photospheric abundance. Thus, in Figure 8 we subtract photospheric abundances from the coronal ones. However, because photospheric abundances are imperfectly known, taking them into account involves numerous assumptions, which we now describe.

In Table 1, photospheric abundances measured for ξ Boo A are listed for C, O, Mg, Si, and Fe. These abundances are quoted relative to solar. The Allende Prieto et al. (2004) analysis from which these abundances are obtained involves a line-by-line comparison of solar and stellar photospheric absorption lines, so these stellar abundances are *fundamentally* relative values. For the purposes of Figure 8, we require absolute photospheric abundances relative to Fe, $\log [X/Fe]_*$, so we have to combine the abundances in Table 1 with some assumed solar abundances. In Figure 8a, we use solar abundances from Grevesse & Sauval (1998).

There are two elements for which no stellar photospheric abundances are available for ξ Boo A: N and Ne. Since these are high-FIP elements, we assume that their abundances relative to the Sun are the same as that of another high-FIP element, O. In other words, we assume $\log[N/N_\odot] = \log[Ne/Ne_\odot] = \log[O/O_\odot] = -0.09$ (see Table 1). For ξ Boo B there are no independent photospheric abundance measurements, so we simply have to assume ξ Boo B is identical to ξ Boo A in this respect. Similar assumptions have been made for the photospheric abundances of ϵ Eri, 70 Oph AB, and 36 Oph AB (see WL06).

The low-FIP and high-FIP data points in Figure 8a are connected with separate dotted lines. These dotted lines indicate the following curious abundance patterns for all the stars: 1. Mg abundances are always higher than those of Si, 2. Ne abundances are always higher than the other high-FIP abundances, and 3. C and N abundances are intermediate between those of O and Ne. Are these abundance patterns telling us something about how coronal fractionation is operating in these moderately active stars? Or are these patterns just a product of assumptions made about the photospheric abundances?

At least for the high-FIP elements, the latter of these two explanations seems most likely. In Figure 8b, we explore this further by changing our assumed photospheric abundances. This figure is like Figure 8a, but instead of Grevesse & Sauval (1998) solar abundances, we

use those of Asplund et al. (2009), with the exception of Ne.

Photospheric Ne abundances provide unique problems, because there are no photospheric Ne absorption lines to measure, which means that solar Ne abundance measurements actually have to rely on emission lines from the corona, where elements are subject to fractionation processes like those that yield the FIP effect. In Figure 8b, we change the assumed photospheric abundance of Ne drastically by assuming that the average coronal Ne/O ratio of $\text{Ne/O} = 0.41$ measured by Drake & Testa (2005) *for active stars* actually represents the real *photospheric* abundance of *all* cool main sequence stars, as opposed to the much lower solar coronal Ne/O ratio of $\text{Ne/O} = 0.17 \pm 0.05$ (Young 2005; Schmelz et al. 2005). In other words, rather than assuming that Ne is fractionated from O in active stars but not in the Sun, in Figure 8b we assume that Ne is being fractionated in the atmospheres of inactive stars like the Sun, but not in active stars. Theoretical support for this interpretation is provided by Laming (2009), and a higher solar photospheric Ne abundance could also help resolve discrepancies between solar interior models and helioseismological observations (Antia & Basu 2005; Bahcall et al. 2005).

With the revised assumptions regarding photospheric abundances discussed above, the high-FIP abundance patterns seen in Figure 8a are largely absent in Figure 8b, and the high-FIP dotted lines are closer to horizontal. This result could be used as evidence in favor of the photospheric abundance assumptions being made in Figure 8b, as opposed to the Grevesse & Sauval (1998) solar abundances being assumed to make Figure 8a.

Although changing the assumed solar abundances seems to be able to significantly reduce the discrepancies among the high-FIP elements, such is not the case for the low-FIP elements, where there is little difference in the discrepancy between Mg and Si in Figures 8a and 8b. Thus, presumably coronal fractionation processes really are enhancing stellar Mg abundances relative to Si in the coronae of these moderately active stars. Laming (2004, 2009) propose that coronal fractionation originates from ponderomotive forces induced by the propagation of Alfvén waves through the chromosphere. These models demonstrate the potential for fractionating Mg relative to Si in a manner consistent with the observed Mg/Si ratios. In their sample of early G dwarfs, Telleschi et al. (2005) also generally find high Mg/Si ratios. But in a sample of M dwarfs, all of which happen to show inverse FIP effects, Liefke et al. (2008) find *low* Mg/Si ratios, suggesting this behavior may be spectral type dependent.

4.6. FIP Effect Variations

For the high-FIP dotted lines in Figure 8, the lower the line, the higher the coronal Fe abundance is relative to the high-FIP elements, and therefore the stronger the inferred FIP effect. Significant FIP effect is apparent for many of the stars, with 70 Oph A’s corona possessing the strongest FIP bias. But there is a significant amount of scatter in the level of FIP effect found for this sample of stars. Figure 8 suggests the following sequence of decreasing FIP bias: 70 Oph A, ξ Boo A, 36 Oph B, 36 Oph A, ξ Boo B, ϵ Eri, 70 Oph B. The last of these stars, 70 Oph B, appears to actually have a slight *inverse* FIP effect.

There is some spread of X-ray luminosity within our sample of stars, but there is no correlation at all between X-ray luminosity and FIP effect in this sample. The most luminous star, ξ Boo A, shows a strong FIP effect, but the second most luminous, ϵ Eri, shows only a weak FIP effect at most. The relatively strong FIP effect of the most active star in our sample also runs contrary to the general anti-correlation between stellar activity and FIP effect that has been reported in the past (see §4.3).

Since the FIP effect on the Sun is latitude dependent, with the effect being strong near the equator and minimal in the polar regions, one might imagine that perhaps stellar orientation could be a factor in the FIP bias observed from a star, assuming coronal abundances on these more active stars also exhibit some sort of latitude dependence. However, since coronal emission is optically thin, at least half of a star’s total emission should be visible from a star regardless of orientation, so it is hard to imagine orientation effects explaining the roughly factor-of-3 variation in FIP bias seen in Figure 8.

In our previous paper (WL06) we have emphasized the remarkable difference between 70 Oph A and 70 Oph B, which represent the FIP effect extremes in Figure 8 despite being similar stars in the same binary system. One possible explanation that we proposed is that perhaps the FIP effect is a time-dependent phenomenon. The solar example provides a precedent for this, with newly emerged active regions having close to photospheric abundances and only acquiring a FIP bias on timescales of days (Widing & Feldman 2001). Thus, for the stars in Figure 8 with little or no apparent FIP bias (e.g., 70 Oph B, ϵ Eri), perhaps the visible surface of the star at the time of observation was dominated by young active regions, whereas the stars with strong observed FIP effects (e.g., 70 Oph A, ξ Boo A) were observed with older active regions. The time-dependent interpretation can only be tested by observing these stars again, preferably more than once. But the limited amount of evidence available so far does *not* support this interpretation. Abundances computed from EUVE spectra taken at different times from our LETGS data seem to be very consistent with our LETGS results, showing a strong FIP effect for ξ Boo A, and only a weak FIP effect, if any, for ϵ Eri (Laming et al. 1996; Laming & Drake 1999). Sanz-Forcada et al. (2003) looked for

abundance variations in multiple observations of the very active K dwarf AB Dor, with the observations encompassing a range of activity levels, and found no such variability.

There does not seem to be a strong case for activity dependence, time dependence, or orientation effects being responsible for the variation in FIP bias seen in Figure 8. There does seem to be a case for there being a spectral type dependence. The two earliest type stars (ξ Boo A and 70 Oph A) have the strongest solar-like FIP effect, while the three latest type stars (70 Oph B, ξ Boo B, and ϵ Eri) have the weakest. This is explored further in Figure 9, where we first compute the average of the high-FIP dotted lines in Figure 8b, a quantity we simply call the “FIP bias,” and then plot this quantity versus spectral type.

In order to broaden the spectral range under consideration, in Figure 9 we supplement our measurements with those of early G stars from Telleschi et al. (2005) and M dwarfs from Liefke et al. (2008). In utilizing measurements from these other papers, we were careful to compute the “FIP bias” in the same manner that we have for our sample of stars, with the same assumptions about solar photospheric abundances as in Figure 8b. For the Telleschi et al. (2005) sample, stellar photospheric abundances are available from Allende Prieto et al. (2004), which we take into account, but for the M dwarfs of Liefke et al. (2008) there are no such measurements and we have no recourse but to assume that the photospheres of these stars possess solar photospheric abundances. Finally, we have added a point for the Sun, using abundances listed in Feldman & Laming (2000).

Figure 9 shows a remarkably tight correlation of FIP bias with spectral type, with the earlier type stars having solar-like FIP effects and the later stars having inverse FIP effects, though the lack of photospheric abundance measurements for the M dwarfs means that conclusions about them are more uncertain. The reversal point seems to happen near spectral type K5 V. To the best of our knowledge, this is the first time a strong spectral type dependence of FIP bias has been claimed. Why has this seemingly strong correlation not been recognized in the past? Answering this question requires clearly defining what the sample of stars in Figure 9 represents. In short, these are inactive to moderately active main sequence stars with X-ray luminosities of $\log L_X \lesssim 29$. For solar-like main sequence stars such stars have rotational periods of $P_{rot} > 6$ days and ages of $t > 0.35$ Gyr (Maggio et al. 1987; Dorren et al. 1995; Güdel et al. 1997; Güdel 2004)

Most surveys of coronal X-ray emission are dominated by interacting binaries, evolved stars, and other targets that represent extremes of coronal activity, which are commonly observed by X-ray telescopes because they are so bright and easy to detect. But by avoiding such extremes and focusing solely on more normal stars, we find a very different empirical view of the FIP effect. Gone is the kind of activity dependence on which previous authors have focused (see §4.3), replaced instead with a strong spectral type dependence. In order

to emphasize the lack of activity dependence in Figure 9, consider the two least active stars in the sample: the Sun (G2 V) and Proxima Cen (M5.5 Ve). The two G1 stars right next to the Sun in the figure have X-ray luminosities almost two orders of magnitude higher than the Sun. But there is no difference in “FIP bias”. Likewise, three of the four stars right next to Proxima Cen in the figure have X-ray luminosities about two orders of magnitude higher than it. Once again, no difference in FIP bias.

There are two stars in the Telleschi et al. (2005) sample that are not included in Figure 9, because they have $\log L_X > 29$ and therefore violate our policy of avoiding extremes. These two stars are 47 Cas B and EK Dra, which both have rotation periods of under three days. This rapid rotation will probably exist for all main sequence stars with $\log L_X > 29$. If we plotted points for 47 Cas B and EK Dra in Figure 9, they would lie well above the relation defined by the other stars. Rather than proposing that magnetic activity is starting to operate somewhat differently at the activity level of 47 Cas B and EK Dra, thereby yielding a different FIP bias, we instead propose that the changes in FIP effect are ultimately driven by changes to fundamental stellar properties induced by the rapid stellar rotation.

Rotation as rapid as that possessed by 47 Cas B and EK Dra will presumably affect the atmospheric and convection zone properties of the star to some extent (e.g., Brown et al. 2008). Interacting binaries and evolved stars will also have substantial differences between their atmospheric properties and those of main sequence stars with identical spectral types. Figure 9 suggests to us that FIP bias is tied directly to basic stellar properties of the star, and not any simple coronal property like total X-ray flux or magnetic field strength. Within the theoretical paradigm of Laming (2004, 2009), in which Alfvén wave propagation through the chromosphere drives coronal abundance anomalies, it is possible to imagine that changes in basic stellar properties such as radius, surface gravity, or convective motions could affect these waves and thereby affect the coronal FIP bias. *In short, we propose that the spectral type dependence of FIP bias in Figure 9 provides a more fundamental insight into the nature and cause of the FIP effect than the activity trends that have been explored in the past.*

5. SUMMARY

We have used *Chandra*/LETGS observations to study the coronae of the ξ Boo binary, and we have compared our results with a previous study of five other moderately active GK dwarfs: ϵ Eri, 70 Oph AB, and 36 Oph AB. Our findings are summarized as follows:

1. The two stellar components of ξ Boo are resolved for the first time in X-rays. We find that ξ Boo A accounts for 88.5% of the counts in the zeroth order image. For

comparison, spectral analysis implies an 84.6% contribution to the system’s X-ray flux in the ROSAT-like 0.1-2.4 keV bandpass.

2. With ξ Boo B detected for the first time in X-rays, we now know it has an X-ray luminosity comparable to stars known to have strong stellar winds, leading to the conclusion that ξ Boo B may account for most of the modest wind observed from the system, with the more active ξ Boo A possessing a surprisingly weak wind despite its active corona. This strengthens the case for the presence of a “wind dividing line” separating moderately active stars with strong winds and very active stars with weak winds, possibly due to the increasing strength of large scale global magnetic fields that inhibit mass loss.
3. Our emission measure analysis of ξ Boo A and B finds evidence for a narrow peak in EM at $\log T = 6.6$ for both stars, a peak also seen for the other moderately active G8-K5 dwarfs in our sample, indicating that the coronal heating mechanism operating on these stars favors this temperature.
4. The emission measure analysis provides us with coronal abundances relative to Fe. Looking for coronal abundance anomalies requires correcting for stellar photospheric abundances, which in turn involves assuming solar photospheric abundances, since the stellar abundances we use are measured relative to solar. When we simply assume solar abundances from Grevesse & Sauval (1998), for our sample of stars we find that the high-FIP element abundances are inconsistent with each other. This inconsistency is decreased significantly for all our stars if we instead assume a photospheric Ne abundance consistent with stellar coronal measurements from Drake & Testa (2005), and solar abundances from Asplund et al. (2009) for other elements. This is an argument in favor of these latter photospheric abundances, unless there are actual coronal fractionation processes taking place among the high-FIP elements that we are erroneously removing.
5. Among low-FIP ions, the coronal Mg/Si ratio is consistently higher than the photospheric ratio for all of our G8-K5 stars, presumably an effect of actual coronal fractionation. An enhancement of Mg relative to Si in the corona is predicted by many of the models of Laming (2009), which are designed to explain solar/stellar coronal abundance anomalies. However, although Telleschi et al. (2005) also finds high Mg/Si ratios for early G dwarfs, coronal Mg/Si ratios appear to be *lower* than photospheric for M dwarfs (Liefke et al. 2008), suggesting a spectral type dependence for this coronal abundance ratio.
6. With regards to the FIP effect, our sample of stars exhibit a range of FIP bias, with

70 Oph A and ξ Boo A having the strongest solar-like FIP effect, ϵ Eri showing little or no FIP effect, and 70 Oph B possessing a slight inverse FIP effect. Expanding our sample of stars even further to include early G stars from Telleschi et al. (2005) and M dwarfs from Liefke et al. (2008), we find that the FIP bias correlates beautifully with spectral type, but only if extremely active stars with $\log L_X > 29$ are excluded.

7. The tight correlation of FIP bias with spectral type suggests to us that the nature and causes of the FIP effect can ultimately be traced directly to fundamental surface properties. Among normal main sequence stars, these change in a very predictable manner with spectral type, explaining the tight correlation in Figure 9. No such correlation exists for extremely active stars, because many are evolved stars with disparate photospheric characteristics, and in other cases the stellar atmospheres will be affected by rapid rotation or the effects of close binarity.

Support for this work was provided by the National Aeronautics and Space Administration through Chandra Award Number GO8-9003Z issued by the Chandra X-ray Observatory Center, which is operated by the Smithsonian Astrophysical Observatory for and on behalf of the National Aeronautics and Space Administration under contract NAS8-03060.

REFERENCES

- Allende Prieto, C., Barklem, P. S., Lambert, D. L., & Cunha, K. 2004, *A&A*, 420, 183
- Antia, H. M., & Basu, S. 2005, *ApJ*, 620, L129
- Arnaud, M., & Rothenflug, R. 1985, *A&AS*, 60, 425
- Asplund, M., Grevesse, N., Sauval, A. J., & Scott, P. 2009, *ARA&A*, 47, 481.
- Audard, M., Behar, E., Güdel, M., Raassen, A. J. J., Porquet, D., Mewe, R., Foley, C. R., & Bromage, G. E. 2001, *A&A*, 365, L329
- Audard, M., Güdel, M., Sres, A., Raassen, A. J. J., & Mewe, R. 2003, *A&A*, 398, 1137
- Bahcall, J. N., Basu, S., & Serenelli, A. M. 2005, *ApJ*, 631, 1281
- Ball, B., Drake, J. J., Lin, L., Kashyap, V., Laming, J. M., & García-Alvarez, D. 2005, *ApJ*, 634, 1336
- Barnes, T. G., Evans, D. S., & Moffett, T. J. 1978, *MNRAS*, 183, 285

- Beuermann, K., Burwitz, V., & Rauch, T. 2006, *A&A*, 458, 541
- Brinkman, A. C., et al. 2001, *A&A*, 365, L324
- Brown, B. P., Browning, M. K., Brun, A. S., Miesch, M. S., & Toomre, J. 2008, *ApJ*, 689, 1354
- Dere, K. P., Landi, E., Mason, H. E., Monsignori Fossi, B. C., & Young, P. R. 1997, *A&AS*, 125, 149
- Dere, K. P., Landi, E., Young, P. R., Del Zanna, G., Landini, M., & Mason, H. E. 2009, *A&A*, 498, 915
- Dorren, J. D., Güdel, M., & Guinan, E. F. 1995, *ApJ*, 448, 431
- Drake, J. J., & Kashyap, V. 2001, *ApJ*, 547, 428
- Drake, J. J., Laming, J. M., & Widing, K. G. 1997, *ApJ*, 478, 403
- Drake, J. J., Peres, G., Orlando, S., Laming, J. M., & Maggio, A. 2000, *ApJ*, 545, 1074
- Drake, J. J., & Testa, P. 2005, *Nature*, 436, 525
- Feldman, U., & Laming, J. M. 2000, *Phys. Scr.*, 61, 222
- Grevesse, N., & Sauval, A. J. 1998, *Space Sci. Rev.*, 85, 161
- Güdel, M. 2004, *Astron. Astrophys. Rev.*, 12, 71
- Güdel, M., et al. 2001, *A&A*, 365, L336
- Güdel, M., Guinan, E. F., & Skinner, S. L. 1997, *ApJ*, 483, 947
- Hartmann, L., Schmidtke, P. C., Davis, R., Dupree, A. K., Raymond, J., & Wing, R. F. 1979, *ApJ*, 233, L69
- Huenemoerder, D. P., Canizares, C. R., Drake, J. J., & Sanz-Forcada, J. 2003, *ApJ*, 595, 1131
- Huenemoerder, D. P., Canizares, C. R., & Schulz, N. S. 2001, *ApJ*, 559, 1135
- Kashyap, V. & Drake, J. J. 1998, *ApJ*, 503, 450
- Kashyap, V., & Drake, J. J. 2000, *Bull. Astron. Soc. India*, 28, 475
- Laming, J. M. 2004, *ApJ*, 614, 1063

- Laming, J. M. 2009, *ApJ*, 695, 954
- Laming, J. M., & Drake, J. J. 1999, *ApJ*, 516, 324
- Laming, J. M., Drake, J. J., & Widing, K. G. 1996, *ApJ*, 462, 948
- Liefke, C., Ness, J. -U., Schmitt, J. H. M. M., & Maggio, A. 2008, *A&A*, 491, 859
- Linsky, J. L., & Haisch, B. M. 1979, *ApJ*, 229, L27
- Maggio, A., Sciortino, S., Vaiana, G. S., Majer, P., Bookbinder, J., Golub, L., Harnden, F. R., Jr., & Rosner, R. 1987, *ApJ*, 315, 687
- Mazzotta, P., Mazzitelli, G., Colafrancesco, S., & Vittorio, N. 1998, *A&AS*, 133, 403
- McKenzie, D. L. 1987, *ApJ*, 322, 512
- Ness, J. -U., Schmitt, J. H. M. M., Burwitz, V., Mewe, R., Raassen, A. J. J., van der Meer, R. L. J., Predehl, P., & Brinkman, A. C. 2002, *A&A*, 394, 911
- Noyes, R. W., Hartmann, L. W., Baliunas, S. L., Duncan, D. K., & Vaughan, A. H. 1984, *ApJ*, 279, 763
- Pandey, J. C., & Srivastava, A. K. 2009, *ApJ*, 697, L153
- Perryman, M. A. C., et al. 1997, *A&A*, 323, L49
- Petit, P., et al. 2005, *MNRAS*, 361, 837
- Petit, P., et al. 2008, *MNRAS*, 388, 80
- Porquet, D., Mewe, R., Dubau, J., Raassen, A. J. J., & Kaastra, J. S. 2001, *A&A*, 376, 1113
- Sanz-Forcada, J., Affer, L., & Micela, G. 2009, *A&A*, 505, 299
- Sanz-Forcada, J., Maggio, A., & Micela, G. 2003, *A&A*, 408, 1087
- Schmelz, J. T., Nasraoui, K., Roames, J. K., Lippner, L. A., & Garst, J. W. 2005, *ApJ*, 634, L197
- Schmitt, J. H. M. M. 1997, *A&A*, 318, 215
- Schmitt, J. H. M. M., & Liefke, C. 2004, *A&A*, 417, 651
- Söderhjelm, S. 1999, *A&A*, 341, 121

- Strassmeier, K. G. 2002, *Astronomische Nachrichten*, 323, 309
- Telleschi, A., Güdel, M., Briggs, K., Audard, M., Ness, J. -U., & Skinner, S. L. 2005, *ApJ*, 622, 653
- Toner, C. G., & Gray, D. F. 1988, *ApJ*, 334, 1008
- Widing, K. G., & Feldman, U. 2001, *ApJ*, 555, 426
- Wood, B. E. 2004, *Living Rev. Solar Phys.*, 1, 2, URL: <http://www.livingreviews.org/lrsp-2004-2>
- Wood, B. E., & Linsky, J. L. 2006, *ApJ*, 643, 444 (WL06)
- Wood, B. E., Müller, H. -R., Zank, G. P., Linsky, J. L., & Redfield, S. 2005a, *ApJ*, 628, L143
- Wood, B. E., Redfield, S., Linsky, J. L., Müller, H. -R., & Zank, G. P. 2005b, *ApJS*, 159, 118
- Young, P. R. 2005, *A&A*, 444, L45

Table 1. Stellar Information

Property ^a	ξ Boo A	ξ Boo B	Refs.
Other Name	HD 131156	HD 131156B	
Spect. Type	G8 V	K4 V	
Dist. (pc)	6.70	6.70	1
Radius (R_{\odot})	0.83	0.61	2
P_{rot} (days)	6.2	11.5	3
$\log L_x^b$	28.86	27.97	4
$\log L_x^c$	28.91	28.17	
\dot{M} (M_{\odot}) ^d	5	5	5
$\log N_H^e$	17.92	17.92	6
$\log [C/C_{\odot}]$	−0.10	...	7
$\log [O/O_{\odot}]$	−0.09	...	7
$\log [Mg/Mg_{\odot}]$	−0.26	...	7
$\log [Si/Si_{\odot}]$	−0.10	...	7
$\log [Fe/Fe_{\odot}]$	−0.26	...	7

^aThe quantities in square brackets are stellar photospheric abundances relative to solar.

^bX-ray luminosities (ergs s^{-1}) from ROSAT all-sky survey data, using the zeroth order LETGS image in Fig. 1 to establish the contributions of the individual stars.

^cX-ray luminosities in the ROSAT-like 0.1–2.4 keV (5–120 Å) bandpass, computed directly from the LETGS spectra in Fig. 3.

^dMass loss rate measurements from astrospheric absorption detections, where the measurement is for the combined mass loss from both stars of the binary.

^eInterstellar H I column density.

References. — (1) Perryman et al. 1997. (2) Barnes et al. 1978. (3) Noyes et al. 1984. (4) Schmitt & Liefke 2004. (5) Wood et al. 2005a. (6) Wood et al. 2005b. (7) Allende Prieto et al. 2004.

Table 2. *Chandra* Line Measurements

Ion	λ_{rest} (Å)	$\log T$	Counts	
			ξ Boo A	ξ Boo B
Si XIII	6.648	6.99	85.5 ± 21.0	< 34.2
Si XIII	6.688	6.99		
Si XIII	6.740	6.99		
Mg XII	8.419	7.11	69.2 ± 17.2	< 31.8
Mg XII	8.425	7.11		
Mg XI	9.169	6.80	207.7 ± 28.1	< 33.2
Mg XI	9.231	6.80		
Mg XI	9.314	6.79		
Ne X	12.132	6.87	362.2 ± 29.9	58.7 ± 15.8
Ne X	12.138	6.87		
Fe XVII	12.264	6.62	110.6 ± 21.8	< 33.4
Fe XXI	12.285	6.98		
Ne IX	13.447	6.58	560.3 ± 38.6	101.4 ± 21.9
Ne IX	13.553	6.58		
Ne IX	13.699	6.58	231.6 ± 28.7	77.0 ± 19.6
Fe XVIII	14.203	6.74	238.0 ± 30.3	< 34.8
Fe XVIII	14.208	6.74		
Fe XVII	15.015	6.59	1033.4 ± 43.8	120.9 ± 20.7
Fe XVII	15.262	6.59	514.9 ± 39.1	58.9 ± 18.6
O VIII	15.176	6.65		
Fe XIX	15.198	6.83		
O VIII	16.006	6.63	465.5 ± 35.1	61.2 ± 18.3
Fe XVIII	16.005	6.73		
Fe XVIII	16.072	6.73		
Fe XVII	16.778	6.58	598.2 ± 32.6	52.7 ± 15.1
Fe XVII	17.053	6.58	1381.5 ± 46.2	134.1 ± 20.8
Fe XVII	17.098	6.58		
O VII	18.627	6.34	76.5 ± 17.4	20.5 ± 13.4
O VIII	18.967	6.59	1227.3 ± 43.1	215.2 ± 22.1
O VIII	18.973	6.59		
O VII	21.602	6.32	307.4 ± 25.5	76.9 ± 17.1
O VII	21.807	6.32	46.7 ± 16.1	14.5 ± 12.5
O VII	22.101	6.31	191.9 ± 22.7	66.5 ± 18.1
N VII	24.779	6.43	83.8 ± 20.9	< 32.0
N VII	24.785	6.43		
C VI	33.734	6.24	152.6 ± 20.9	41.6 ± 15.5
C VI	33.740	6.24		
S XIII	35.667	6.43	45.3 ± 18.7	< 30.0
Si XI	43.763	6.25	78.5 ± 19.0	14.0 ± 12.2
Si XII	44.019	6.44	87.5 ± 17.6	24.7 ± 13.0
Si XII	44.165	6.44	183.3 ± 23.7	40.1 ± 16.8
Si XII	45.521	6.44	46.9 ± 18.1	< 30.4
Si XII	45.691	6.44	96.3 ± 18.1	< 31.4
Fe XVI	46.661	6.43	75.1 ± 20.2	< 30.8
Fe XVI	46.718	6.43		

Table 2—Continued

Ion	λ_{rest} (Å)	$\log T$	Counts	
			ξ Boo A	ξ Boo B
Si XI	49.222	6.24	95.5 ± 20.2	23.9 ± 13.9
Fe XVI	50.361	6.43	202.6 ± 24.0	13.3 ± 11.5
Fe XVI	50.565	6.43	80.5 ± 17.8	< 27.4
Si X	50.524	6.15		
Si X	50.691	6.15	16.8 ± 13.0	< 25.8
Si XI	52.298	6.24	27.6 ± 13.6	< 26.4
Fe XV	52.911	6.32	33.4 ± 14.3	< 24.8
Fe XVI	54.127	6.43	48.2 ± 15.9	< 27.2
Fe XVI	54.710	6.43	115.4 ± 19.1	< 25.4
Mg X	57.876	6.22	101.0 ± 20.2	< 29.4
Mg X	57.920	6.22		
Fe XV	59.405	6.32	45.3 ± 15.1	< 29.2
Fe XVI	62.872	6.42	54.5 ± 13.4	< 26.0
Mg X	63.295	6.21	55.6 ± 13.4	< 26.6
Fe XVI	63.711	6.42	94.1 ± 17.7	15.3 ± 10.6
Fe XVI	66.249	6.42	188.6 ± 23.2	< 27.4
Fe XVI	66.357	6.42		
Fe XV	69.682	6.32	137.0 ± 19.5	24.5 ± 12.5
Fe XV	69.941	6.32	59.1 ± 18.0	< 29.4
Fe XV	69.987	6.32		
Fe XV	70.054	6.32		
Mg IX	72.312	6.02	30.0 ± 13.4	19.0 ± 11.7
Fe XV	73.472	6.32	74.4 ± 18.4	19.5 ± 11.8
Fe XVI	76.497	6.42	46.6 ± 14.6	< 28.6
Ne VIII	88.082	5.96	65.5 ± 16.5	35.0 ± 15.8
Ne VIII	88.120	5.96		
Fe XVIII	93.923	6.68	309.2 ± 29.5	25.0 ± 16.7
Ne VIII	98.116	5.94	45.6 ± 18.0	< 40.2
Ne VIII	98.260	5.94	62.1 ± 21.0	27.2 ± 19.3
Fe XIX	101.550	6.80	35.5 ± 17.5	< 39.0
Fe XVIII	103.937	6.68	84.2 ± 21.6	< 38.8
Fe XIX	108.355	6.79	158.5 ± 25.5	< 40.2
Fe XXII	117.180	7.03	75.0 ± 22.6	< 39.6
Fe XX	121.845	6.88	60.7 ± 18.5	< 39.8
Fe XXI	128.752	6.95	46.2 ± 18.0	< 40.8
Fe XX	132.840	6.88	138.8 ± 26.3	< 39.2
Fe XXIII	132.906	7.12		
Fe IX	171.073	5.95	31.0 ± 16.4	27.2 ± 17.9

Table 3. Coronal Densities and Abundances

	ξ Boo A	ξ Boo B	Sun ^a
$\log n_e$	< 10.24	< 11.43	9.4
$\text{Fe}/\text{Fe}_\odot$	0.7	0.8	1
$\log [\text{Fe}/\text{H}]$	−4.65	−4.60	−4.50
$\log [\text{C}/\text{Fe}]$	$0.75^{+0.09}_{-0.07}$	$0.87^{+0.28}_{-0.34}$	1.02
$\log [\text{N}/\text{Fe}]$	$0.19^{+0.11}_{-0.17}$...	0.42
$\log [\text{O}/\text{Fe}]$	$1.02^{+0.03}_{-0.03}$	$1.13^{+0.12}_{-0.12}$	1.33
$\log [\text{Ne}/\text{Fe}]$	$0.58^{+0.02}_{-0.03}$	$0.87^{+0.09}_{-0.15}$	0.58
$\log [\text{Mg}/\text{Fe}]$	$0.23^{+0.08}_{-0.06}$	$0.22^{+0.38}_{-0.98}$	0.08
$\log [\text{Si}/\text{Fe}]$	$0.04^{+0.07}_{-0.07}$	$0.20^{+0.18}_{-0.36}$	0.05
$\log [\text{S}/\text{Fe}]$	$-0.28^{+0.24}_{-0.57}$...	−0.17

^aThe coronal density quoted for the Sun is from McKenzie (1987), while the abundances listed are photospheric abundances from Grevesse & Sauval (1998).

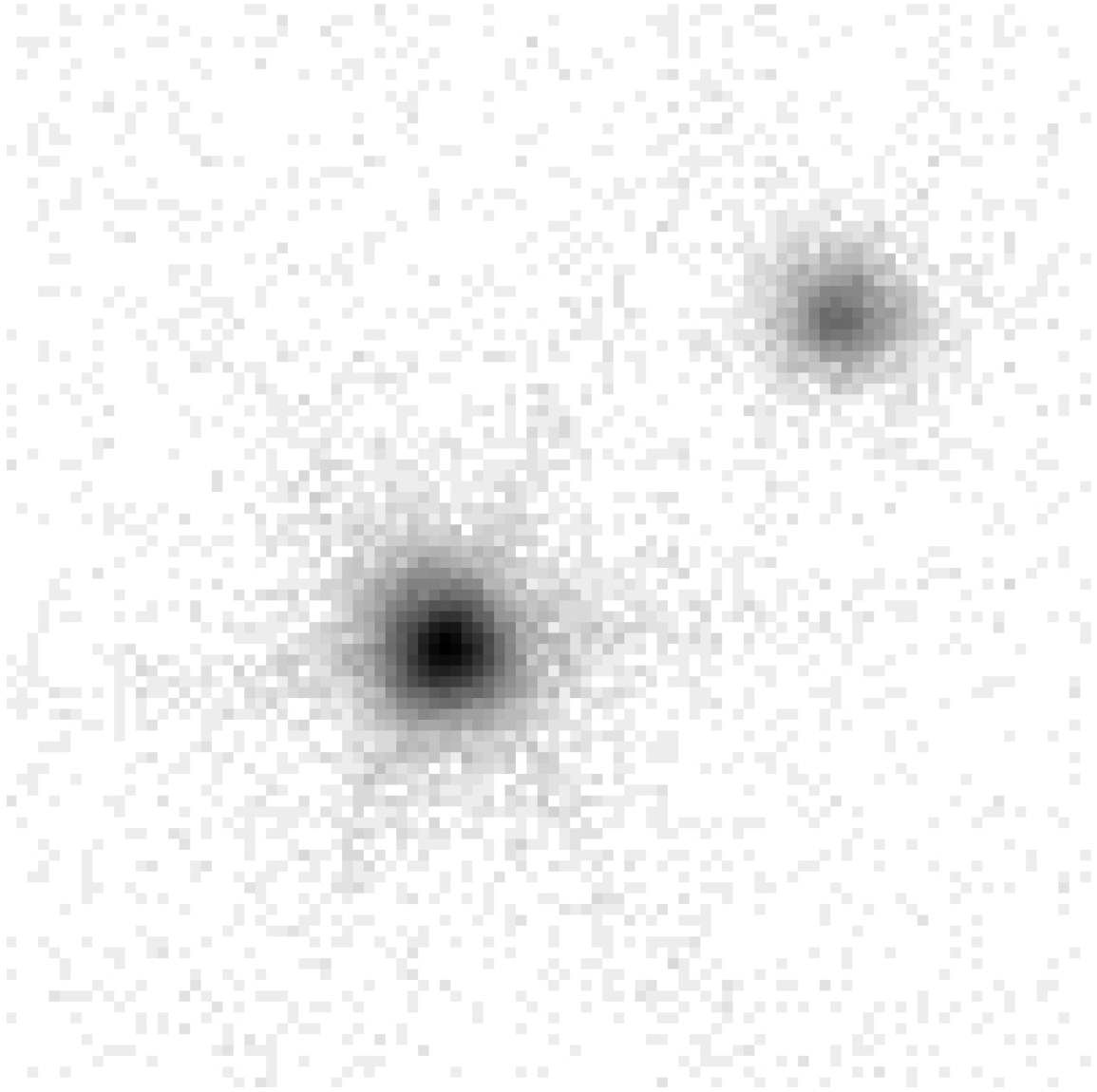


Fig. 1.— Zeroth-order image of the ξ Boo binary (G8 V+K4 V) from a *Chandra* LETGS observation, with north being up in the figure. The brighter G8 V component of the binary accounts for 88.5% of the system’s total X-ray counts. The stellar separation is $6.30''$.

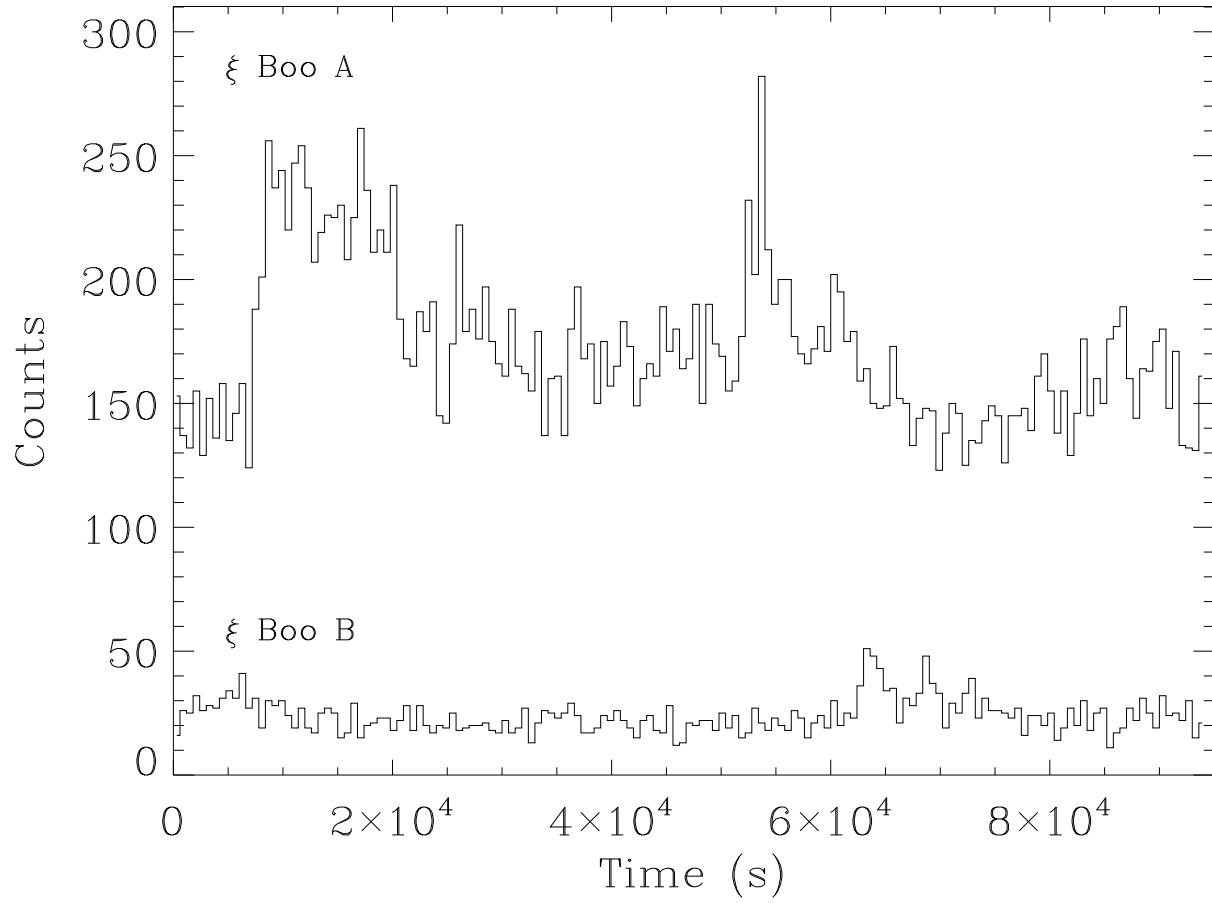


Fig. 2.— X-ray light curves for ξ Boo A and B measured from the zeroth-order images in the *Chandra* LETGS data, using 10 minute time bins.

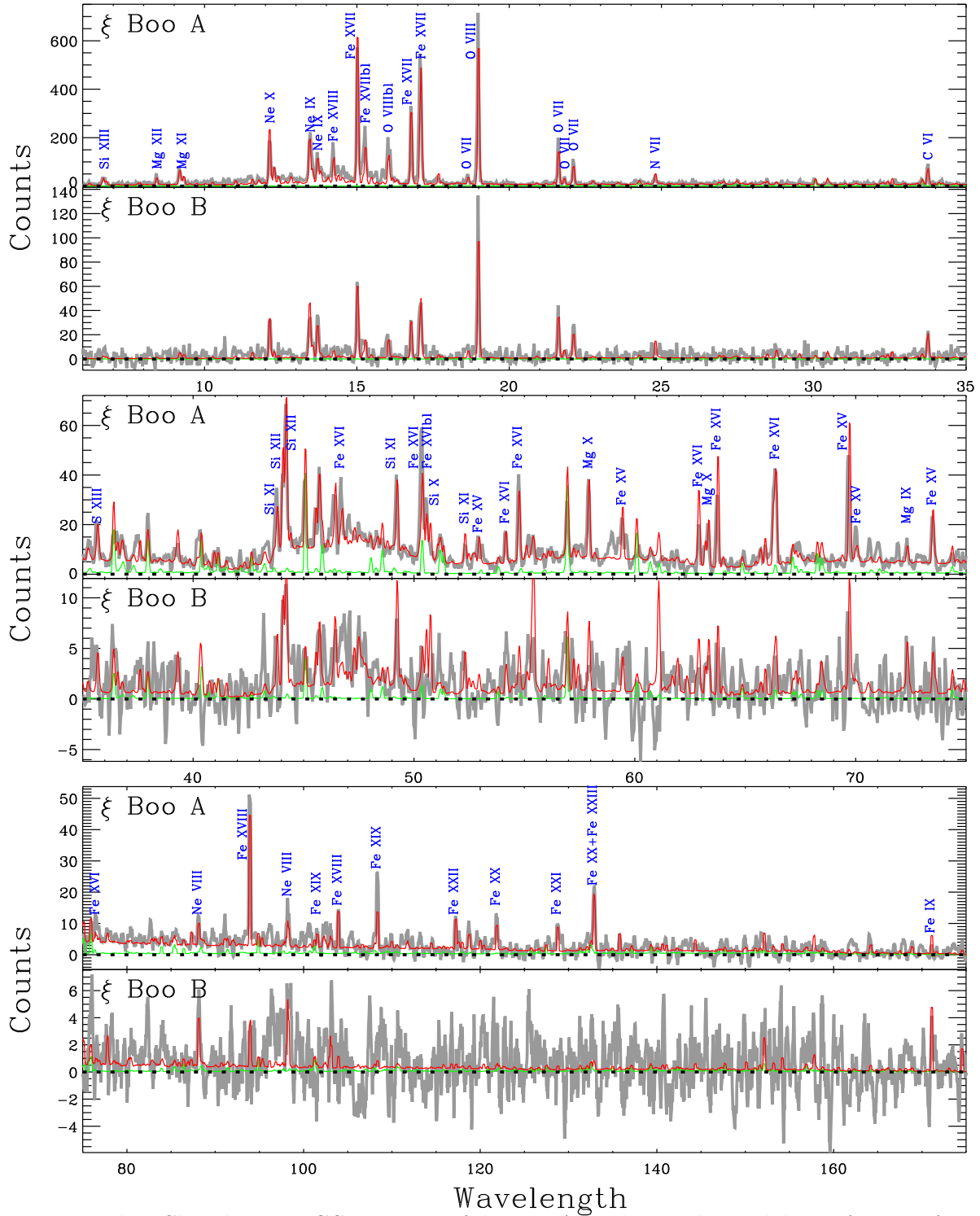


Fig. 3.— The *Chandra* LETGS spectra of ξ Boo A and B, rebinned by a factor of 3 to improve S/N. For wavelengths above 35 Å, the spectra are also smoothed for the sake of appearance. The red lines are synthetic spectra computed using derived emission measure distributions (see Fig. 6), and the green lines indicate the contributions of higher spectral orders (2–5) to the model spectra.

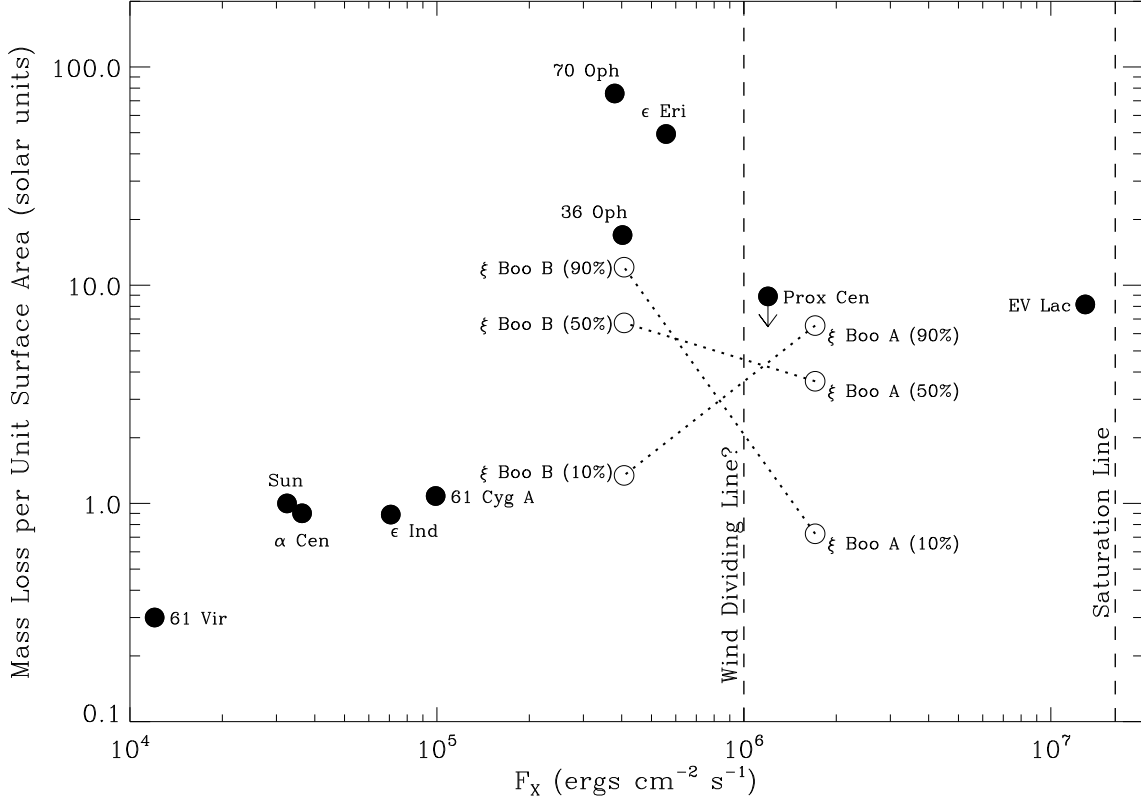


Fig. 4.— Mass loss rates (from Wood et al. 2005) plotted versus X-ray surface flux for various main sequence stars. Since only ξ Boo’s total mass loss rate is known, points are plotted for ξ Boo A and B assuming 3 different divisions of wind between the two stars. Only if ξ Boo B accounts for most of the binary’s wind is ξ Boo B consistent with similar stars (especially 36 Oph). In this instance ξ Boo A’s wind would have to be very weak, strengthening the case for a “wind dividing line” marking where the relation between coronal winds and X-ray emission changes dramatically.

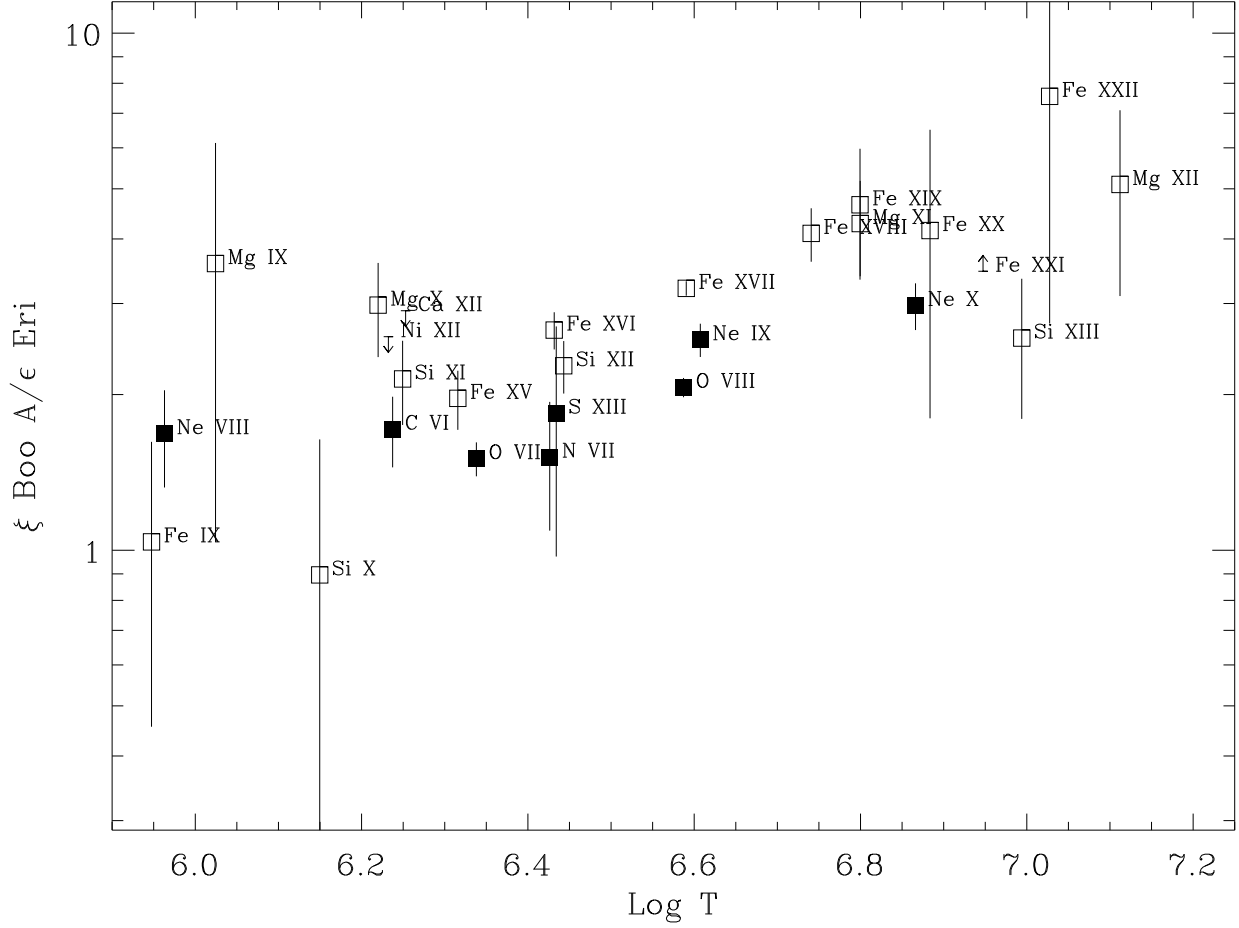


Fig. 5.— ξ Boo A/ ϵ Eri line luminosity ratios for emission lines detected for both stars, plotted versus line formation temperature. The observed ratios above one indicate that ξ Boo A is somewhat more active than ϵ Eri at all temperatures. The ratios smoothly increase with temperature, implying a hotter corona for ξ Boo A. Higher ratios are clearly observed for lines of low FIP elements (open boxes) than for high FIP elements (filled boxes), indicating that the corona of ξ Boo A has a stronger FIP effect than ϵ Eri.

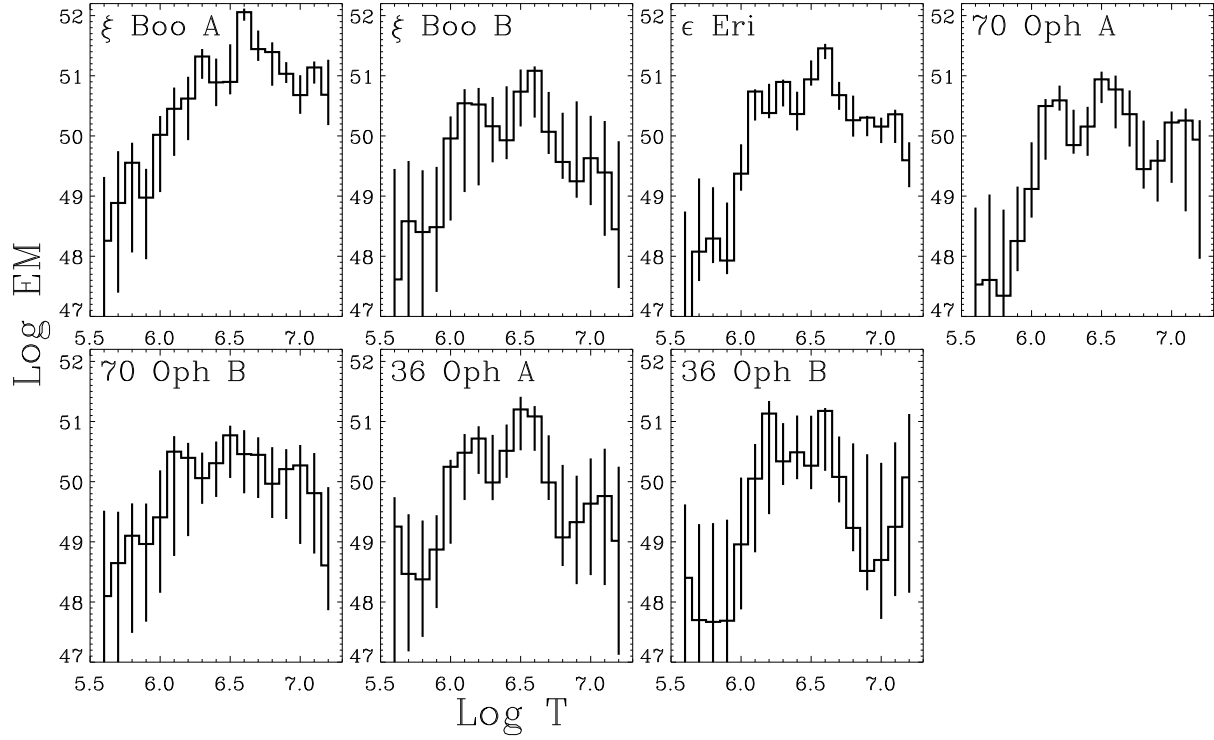


Fig. 6.— Emission measure distributions derived for seven moderately active G8-K5 dwarfs observed by *Chandra* LETGS, with 90% confidence error bars. The ξ Boo AB analyses are from this paper, while the other five are from WL06. Note the peak near $\log T = 6.6$ seen for all these stars.

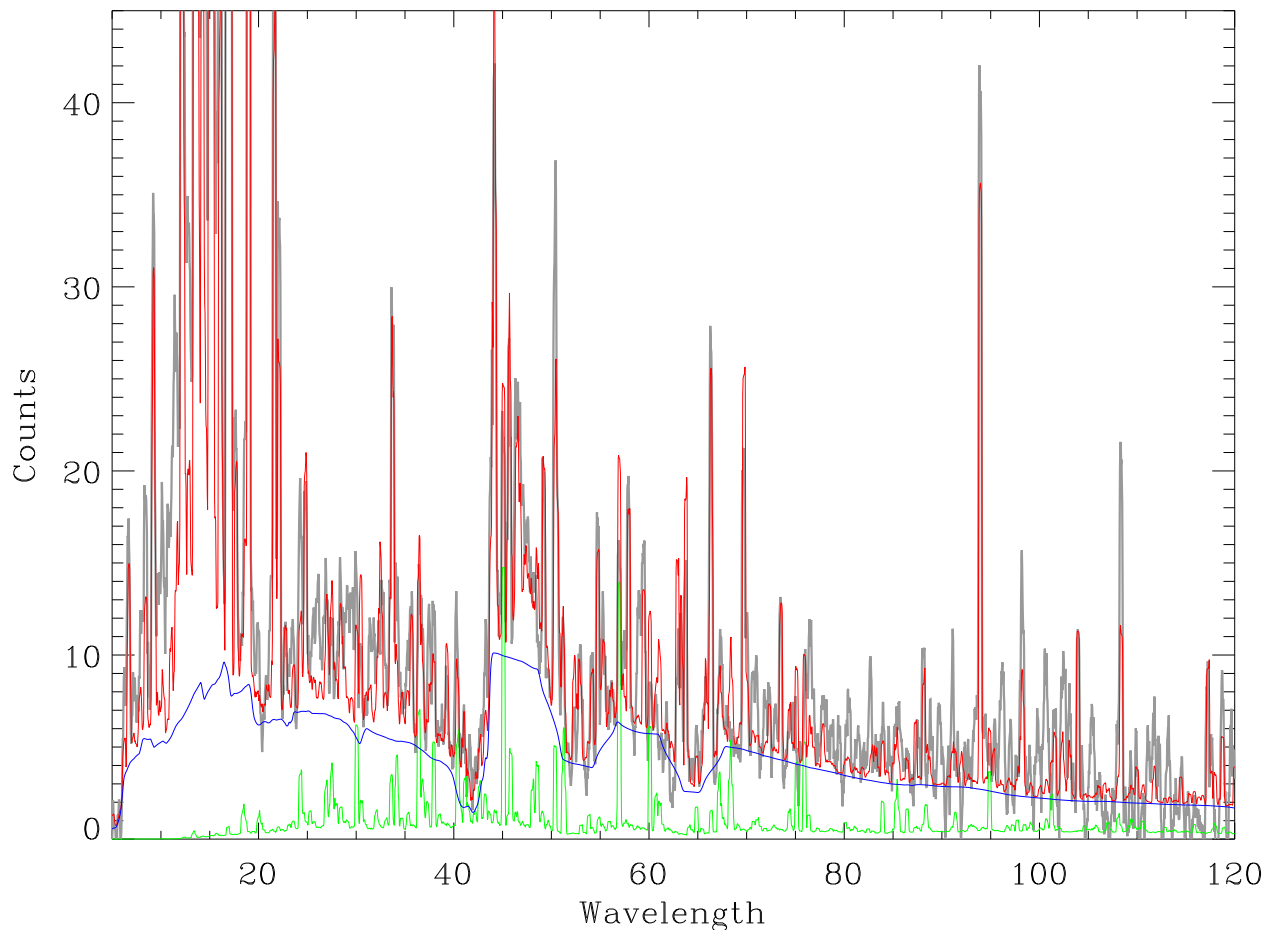


Fig. 7.— A synthetic spectrum (red line) showing our best fit to the highly smoothed *Chandra* ξ Boo A spectrum (gray line). Line contributions are computed from the emission measure distribution in Fig. 6. The continuum contribution to the total spectrum (blue line) assumes an absolute Fe abundance of $[\text{Fe}/\text{H}] = 0.7[\text{Fe}/\text{H}]_{\odot}$. The green line shows the contributions of higher spectral orders (2-5) to the total spectrum.

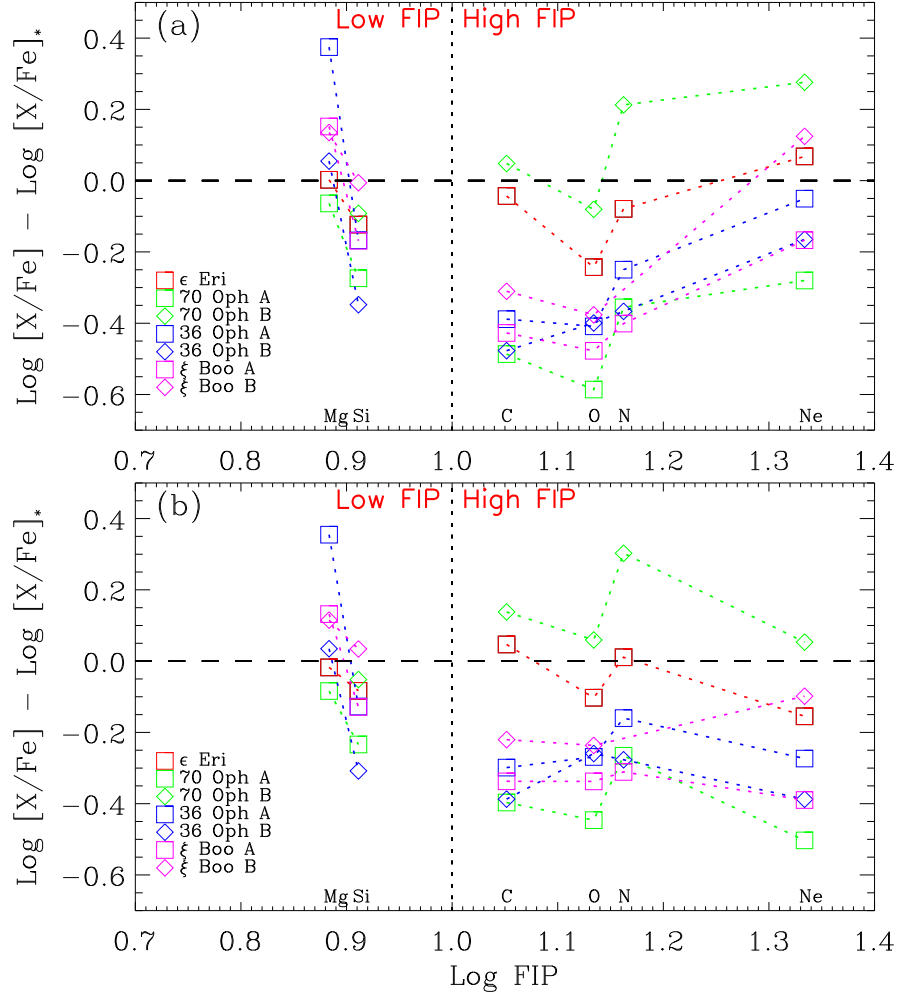


Fig. 8.— (a) Coronal abundances of various elements relative to Fe plotted versus FIP (in eV), for seven moderately active G8-K5 dwarf stars. The abundance ratios are shown relative to assumed stellar photospheric ratios ($\text{log} [X/\text{Fe}]_*$). The vertical dotted line separates low-FIP and high-FIP elements, and colored dotted lines connect the abundances for each star within these two regimes. The high-FIP abundance levels suggest the following sequence of increasing FIP effect: 70 Oph B, ϵ Eri, ξ Boo B, 36 Oph A, 36 Oph B, ξ Boo A, 70 Oph A. (b) Same as (a), but with different assumptions about the photospheric abundances. Instead of Grevesse & Sauval (1998) as the source of solar abundances, we here use Drake & Testa (2005) for Ne, and Asplund et al. (2009) for other elements. With these new assumptions, the high-FIP dotted lines are more horizontal, and therefore more self-consistent, possibly indicating that the photospheric abundances assumed here are better than in (a).

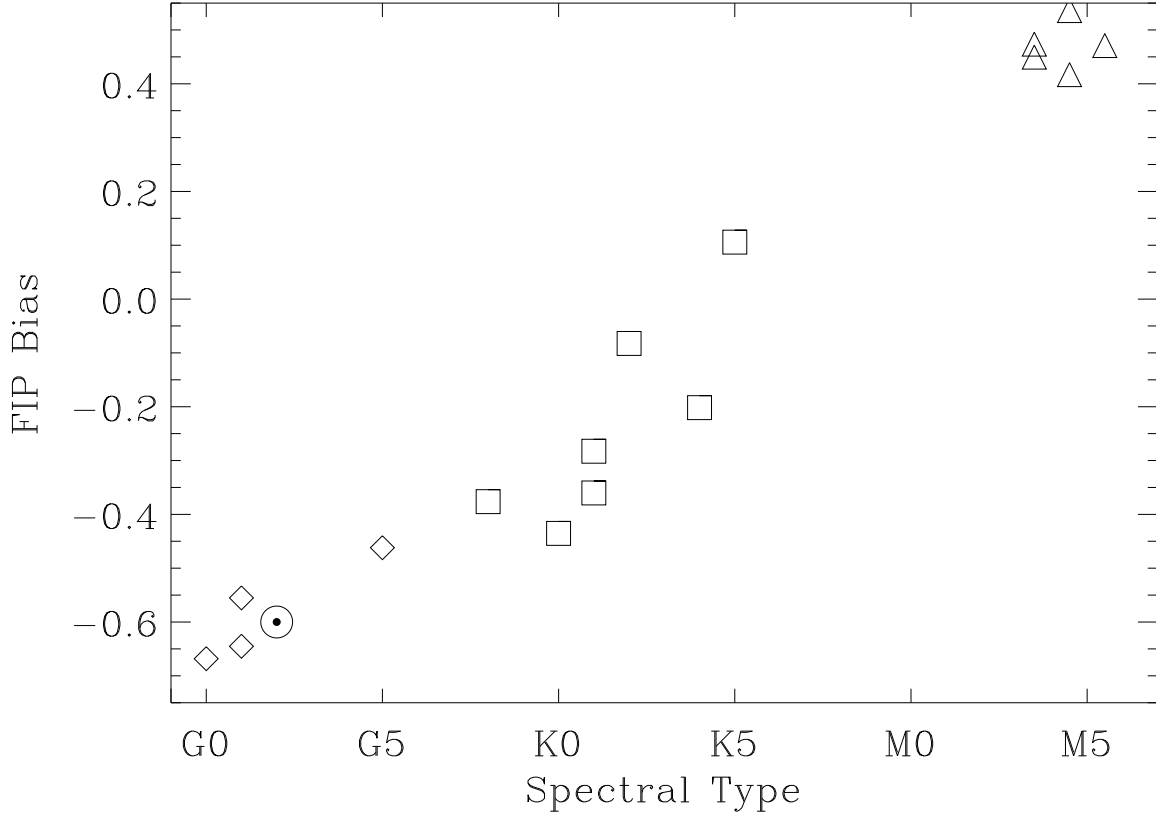


Fig. 9.— The boxes indicate the average values of the high-FIP curves from Fig. 8b, here simply called the “FIP bias,” plotted versus spectral type. We supplement our measurements with ones from Telleschi et al. (2005) (diamonds) and Liefke et al. (2008) (triangles), in addition to a solar value from Feldman & Laming (2000). For all the GK stars the FIP bias calculations include corrections for stellar photospheric abundances from Allende Prieto et al. (2004), but for the M stars there are no stellar photospheric measurements available so we have to simply assume solar photospheric abundances apply. The uniform assumption of abundances other than solar photospheric for the M dwarfs could potentially affect the consistency of the M dwarfs with the correlation defined by the other stars. For purposes of this figure, we avoid extremes of stellar activity, confining our attention to stars with $\log L_X < 29$.